On-chip mobile microrobotic transducer for high-temporal resolution sensing using dynamics analysis

Hugo Salmon, Laurent Couraud, Gilgueng Hwang

Version of Record: https://www.sciencedirect.com/science/article/pii/S0924424718313049
Manuscript_28015b9875df58c178b3b511a5740405

On-chip mobile microrobotic transducer for high-temporal resolution sensing using dynamics analysis

Hugo Salmon[a,1], Laurent Couraud[a], Gilgueng Hwang[a,*]

[a] *Centre for Nanoscience and Nanotechnology, French National Research Center (CNRS), Route de Nozay, Marcoussis 91460, France*

Abstract

Untethered mobile magnetic microrobots in liquids are under increased investigation with the intended goal to obtain *in-vivo* transducing applications, mostly for micromanipulation or cargo transport. Using them as wireless sensors is less common though it offers a highly controllable and mobile sensing capability at micrometric scale with the capability to provide information about their dynamics and interaction with their environment. Here a system is proposed which is fully controllable by calibrated external magnetic fields and high temporal resolution ($> 5000FPS$) visual feedback. With the targeted applications being in microscale fluids, a mobile magnetic microrobot is integrated into an optically transparent microfluidic chip which demonstrates sensing capabilities. In these experiments, physical sensing is quantified through microrobot dynamics analysis of its elementary planar motions (rotary and translational) and these results are related to local viscosity of fluid and friction from the interfaces. These results also allow for the characterization of swimming performances, magnetization and thus help to improve the design of the microrobotic system. An analysis of transition dynamics also provides complementary measurement

*Corresponding author
Email addresses: hugo.salmon@gmail.com (Hugo Salmon), gilgueng.hwang@c2n.upsaclay.fr (Gilgueng Hwang)
URL: https://sites.google.com/site/gilguenghwang/home (Gilgueng Hwang)
[1]Present address: McGill University, Genoma Building, Dept. of Biomedical Engineering, 740 Dr. Penfield Drive, Room 4300, Montréal, QC H3A 0G1, CANADA

on the microrobot hydrodynamics and the interaction with its substrate. The proposed on-chip mobile microrobotic system provides an advantageous testing platform to further investigate the visual servo automation control towards their *in-vitro* or *in-vivo* applications.

Keywords: Magnetic mobile microrobots; microrobotic sensing; micromanipulation; microfluidics Submission no: SNA_2018_1236

Highlights

- upgraded control with fast visual feedback using optical microscopy coupled to real-time object tracking
- translational sensing: backward/forward translational motions and their substrate influences
- rotary sensing: breakdown phenomenon provides an access to on-chip integrated local viscometry and magnetometry

1. Introduction

Untethered mobile microrobots for biomedical applications have been a growing interest for the last decade [1, 2], particularly in liquids environment [3, 4], corresponding to most of biological applications. They could offer artificial theranostic tools and their applicative potential remains of high interest. Unlike natural biological microswimmers [5, 6], they can be easily manufactured taking advantage of microelectronics process and provide a high precision transducing tool. However, microrobotic systems are subject to the predominance of surface effect: sticking forces (surface tension, Van der Waals interaction, electrostatic, roughness) - common scale effects [7] leading to unpredictable dynamics [8], as well as liquid viscosity which leads to heavily damped motions [9, 10]. As a result, microrobots interaction with their environment require further investigation and more control.

If knowing more about the microborobot structure itself and its swimming method is still of great interest, its environment and how it interacts with it has not been much explored. Environments such as microfluidic chips offer interesting highly controllable and reproducible experimental frameworks to study robots hydrodynamics [11, 12] and develop *in-vitro* applications such as single cell manipulation [13]. Taking advantage of microrobot dynamics, it is possible to achieve remote interaction taking advantage of periodic motion such as rotation [14] or vibration[15].

Microrobotic in confined microchannels on chip has several advantages:

- reduced contamination and good repeatability [10]
- easy instrumentation
- simplified visual monitoring
- precise control of physical and chemical external conditions
- enhanced controllability of surface chemistry and roughness (surface treatment, channel section control)

A vast amount of design, material and fabrication processes keep emerging, providing technologies tailored to targeted applications [16].

Using mobile microrobots as a sensor is less common at microscopic scale while it could serve as a highly controllable and mobile sensor of its micrometric environment [17]. Indeed, they already provide sensing capacities with living matter *in-vitro* such as yeast [18], oocytes [13, 19], erythrocyte [20, 21, 22] and display a high potential for *in-vivo* applications as well [23]. Though some physico-chemical sensing such as pH measurement[24] or O_2 concentration[25], most of these applications focus on force sensing measuring induced stress of the robot on flexible material.

Getting more information from hydrodynamics could also lead to better characterizations of microrobots and their interaction with liquids media as well as phase boundaries (surface tension for liquid-liquid or liquid-air, and electrostatic forces and roughness for liquid-solid). Among existing sensing methods, it can mentionend at nanometric scale ($< 1\mu m$) that monitoring brownian and rotary motion of nanoparticles has led to measure chemical and physical properties of the particles themselves, from size to conformation analyzing their brownian motion[26] as well as their environment rheology and torque spectroscopy for rotary motion[27]. At micrometric scale, some μTAS and microfluidic devices embed sensing capacities based on the kinectif of mechanical beams[28], beads[29] or droplet geometry[30]. Most current robot dynamics studies focus

on corkscrew motions, investigating the relation between rotary and translational motions [4, 31]. Exploring their swimming strategy also allows for the development of new micromanipulation strategies[17, 11, 32]

We here describe MagPol (for Magnetically polarizable) [33] (see graphical abstract), a mobile magnetic microrobot (3M) taking advantage of its ferromagnetic magnetization, integrated in a microfluidic environment previously introduced at IEEE International Conference on Robotics and Automation [34] microrobotic competition and considerably improved since. More information is collected on the micro-environment and robotic systems through high temporal resolution ($> 5000FPS$) dynamics analysis taking advantage of an optically transparent microfluidic chip, transmission lighting and detection algorithm. The microrobot is fully controllable by an optimized external magnetic field using gradients or a uniform magnetic field, giving access to wide range of motion - including vertical motion and tumbling - and power. Its sensing capabilities are demonstrated through rotary motion dynamics and extend to translational motions. In particular, taking advantage of its polarization compared to the magnetic field direction, backward and forward motion can be compared. Due to its robustness to a wide range of physical conditions, the MagPol can be used to detect the liquid characteristics of unknown, thus hazardous, fluid as well as determining its own 3M hydrodynamic performances. Finally, we provide analysis of transition dynamics, providing a complementary analysis to understand the complex surface phenomenon of the microrobot with its environment.

2. Material and methods

2.1. Chemicals & materials

Chemicals reagents were obtained from Sigma-Aldrich (Breda, The Netherlands). Solvents were purchased from Carlo Erba (Val-de-Reuil, France). RTV 615 polydimethylsiloxane (PDMS) was purchased from Momentive (Columbus, OH). MIF developer were obtained from Microchemicals (Ulm, Germany). LOR5A, SU-8 2050 and 2075 were obtained from Microchem (Westborough,

MA, USA). Glass wafers were obtained from Corning (Bagneaux-sur-Loing, France) and Si wafers from Sil'tronix (Archamps, France). Polymer photomasks were printed by Selba (Versois, Switzerland). Harrick plasma cleaner PDC 32G-2 (Ithaca, NY, USA) could generate 0_2 plasma permanent bonding. Fluidic connections and tubing were obtained from Cluzeau Info Labo (Sainte-Foy-La-Grande, France). The pressure controller was an AF1 from Elvesys (Paris, France). The electrical connections were purchased at RadioSpare (Beauvais, France). Electrical power source was a Keithley 2400 sourcemeter SMU instrument. Biopsy punch were from VWR.

2.2. Microfabrication, from Cr mask lithography to MagPol integration and assembly on chip

The MagPol mask had close to microns details, *Cr* masks were used to achieve optical lithography. A LEICA EBPG 5000+ electron lithography exposed a PMMA layer over a Pyrex thick substrate (2mm) to transfer the patterns. The PMMA photoresist was developped and a thin *Cr* layer was evaporated on it using a Plassys MEB 550 SL. A lift-off process allowed us to develop in acetone the structure and obtain the pattern on a *Cr* mask. A $525\mu m$ *Si* wafer was cleaned successively in 1,1,2-Trichloroethene at 60°C , 2-Propanol at room temperature and deionized water, then dried using air gun. Firstly, a PMMA sacrificial layer using standard spinning and baking was spin-coated on a clean wafer. Secondly, a *Cr* layer of $30nm$ was evaporated for adhesion purpose, followed by a *Ni* layer of $100nm$. SU-8 2050 was spun at $500rpm$ for $5-10s$ with acceleration of 100 rpm/second, then spun at $4000rpm$ for $30s$ with acceleration of $300rpm/s$. It was soft baked 2min at 65°C , 5min at 95°C, then cooled down to RT. Light exposure was done using a MJB-4 lithography using a $310-320$nm standard bandwidth optical filter to transfer *Cr* masks. Post exposure bake was done 1min at 65°C , 6min at 95°C, then cooled down to RT. Development was achieved using SU-8 developer for $4-5$min. Hard baking was done 1h at 150°C. The electrolytic growth of *Ni* over the conductive layer was achieved in a *Ni* $0.1M$ electrolytic bath (composed of a $NiSO_4$ 26.2g/L, $NiCl_2$

3.5g/L and H_3BO_3 3.1g/L). The sample constituted the anode and a second electrode was placed at a 1cm distance with a spiral shaped Pt wire. They were both connected to a generator which induced a current in the direction of the platinum electrode and the solution was agitated for 2hours. Finally, a lift-off using trichloroethylene released the microrobot which then were collected and rinsed by filtration of the solution. Final thickness of the microrobot could reach up-to $10\mu m$.

A Si wafer was cleaned in a similar manner for the microchip fabrication as for the microrobot. SU-8 2050 was spun at $1500rpm$ to obtain $\approx 100\mu m$ thick structures. It was soft baked 5min at 65°C , 20min at 95°C, then cooled down to RT. Light exposure was done by MJB-4 lithography using a $310 - 320nm$ standard bandwidth optical filter transferring polymer photomasks patterns. Post exposure bake was done for 5min at 65°C , 12min at 95°C, then cooled down to RT. Development was achieved using an SU-8 developer for $10-15$min. Hard baking was done for 20min at 150°C. The obtained mold was cleaned, and PDMS was poured on it in a Petri dish. After vacuum degassing for 1h, it was baked in an oven at 85°C. A polished glass wafer was used as the substrate combined with PDMS and cleaned using piranha solution ($H_2SO_4$95%, $H_2O_2$30% , 2:1). The chip substrate was diced using a saw-dicing machine (ESEC8003). Each of the input holes were punched using a biopsy punch. The microrobot body was picked up and dropped at the center of the main fluidic chamber using a dust free wiper. To achieve permanent bonding of the chip, PDMS molded layers were exposed to O_2 plasma (20sccm, 50mT for 2min, 300W) then sealed them on diced slides. Steel pins were inserted for chip-to-tube interface $0.025OD \times 0.017ID$, 0.500" length, in PDMS walls to generate a flow in the chip and renew the solution.

Microrobot and microchannels geometries were monitored througout the different fabrication steps using scanning electron microscopy, which was achieved on a Hitachi S4800 and mechanical profilometry achieved on a Dektak 3ST.

2.3. Helmholtz coils calibration, FEM electromagnetic simulation

Helmholtz and gradient coils magnetic flux were simulated using a 3D finite element method (FEM) model, achieved on Comsol Multiphysics 4.3a from Comsol Lab (Grenoble, France) using AC/DC module. Geometry and wiring were identical to the fabricated coils from the mechanical device used for microrobot magnetic control. The electrical circuit was run by 1 A current. Simulation borders were in a square perimeter of $1 \times 1m^2$. The analyses were achieved using a free quad mesh with an extremely fine definition. Calibration was achieved placing a hall effect probe at the center of the Helmholtz device held by a mechanical arm. Each axis was calibrated separately, first by finding the optimal angular position of the probe in the coils axis direction, and secondly by measuring a range of magnetic flux varying electrical power.

2.4. Microrobot magnetic open loop control and dynamics analysis

Polymer and metallic mechanical supports were fabricated with a three-dimensional printer and a computer numerical control (CNC) milling machine. Wiring of coils and assembly were completed at our mechanical workshop and two types of magnetic setups were developed. Helmholtz pair of coils induced exclusively uniform field on 3 axes X, Y and Z, inducing exclusively a magnetic torque over ferromagnetic particles. Gradient electromagnets on +X, -X, +Y and -Y had a permalloy core to minimize hysteresis and eddy current losses. They allowed for the obtainment of a higher magnetic flux in the axial direction of each coil. The superposition of the emitted magnetic flux induced a pulling force in each direction of the plane. A defined range of frequency including the cut-off frequency was generated and amplified at a sub-millisecond (200μs) sampling rate. Magnetic coils were voltage-controlled through a data acquisition card (S626 Sensoray, $5kHz$ sampling frequency) and amplified through Maxon Motor LSC 30/2 50 W servomotor controller (Neyron, France) 50W power $\mid V \mid <$ 10V and $I <$ 2A. Transmission lighting was achieved using a fiber optic visible light illuminator. When it is connected to an Optronis CL600x2 CMOS camera, it can deliver a bandwidth 655GB/s i.e. 5000 fr /s with

a $512 \times 268 px^2$ resolution. Control was achieved on our custom-built software platform including a parallel control of visual feedback and magnetic actuation and a graphical user interface (GUI). If nothing was specified, analyses were achieved in 20% isopropyl alcohol diluted in milliQ water medium, allowing for the maintenance of a sterile and chemically clean chamber and the facilitation of bubble evacuation.

All trajectories were achieved at constant pressure, in a renewing chamber in case of bubble contamination. For translational motion analysis, every trajectory started from the opposite side of the chip, with fixed orientation of the robot. For rotary motion analysis, the robot was maintained close from the chamber center. A $C\#$ program was developed treating simultaneously signal emissions and high-throughput data acquisition. Image processing was achieved using ImageJ, an open source imaging software (ImageJ [35]). From the post-processed images, trajectories, kinetics and dynamics could be deduced using an open source visual servoing platform library (ViSP) blob tracker [36] for shape detection and moving-edge tracker for edge detection. To determine the cut-off frequency, the $< \Omega >$ of the robot was measured on 10 magnetic cycles to detect the breakdown phenomenon in a reproducible manner. The frequency response scan defined the temporal resolution. The cut-off was defined as the highest frequency with an average rotation rate $< \Omega >$ equals to field pulsation ω_c. A first scan was performed with 10 Hz step to detect the rough cut-off frequency, and then a more precise cut-off frequency was obtained with 1 Hz step zoom centered on the value. Another strategy for quicker convergence could be done using such a dichotomy. It was essential to calibrate the electromagnetic coil setup prior to the rotary or translational dynamics measurements. All data analysis and plots were achieved with Matlab 8.1. Supporting information provide more details of control and imaging processing in SI1 section.

3. Results and discussion

3.1. Integrated ultra-thin ferromagnetic microrobot in soft microfluidics

The MagPol inside microfluidic device was fabricated based on MEMS process described in Figure 1 schematics. It displayed several improvement compared to [33] and its fabrication is fully detailed in Methods section. With usual bottom-up techniques, including lithography and electroplating on a Cr/Ni substrate, its body consisted in a $50nm$ Cr and a $5-10\mu$m Ni ferromagnetic layer. In all of our experiments, final thickness was $\approxeq 5\mu m$ but it could be tuned thanks to electroplating method, above $10\mu m$, the Ni growth was limited by delamination and high surface roughness. The Ni growth layer was $100nm$ to increase conductivity and minimize Joule effect. This was critical to improve the grown material density, roughness and allowed to grow a thicker 3M body. Morover, the PMMA sacrificial allowed to avoid using time consuming and costly ion beam etching compared to former art. The important volume of ferromagnetic material allowed for higher magnetization, development of a wider range of dynamics and thus wider sensing range as can be seen further in our context.

The robot's axes of symmetries define the magnetization direction. The robot's design - as seen on Figure 2 pictures - defined a clear horizontal axis following the arms' direction. It also had the advantage of being easily trackable for both edge and shape tracking algorithm. The transparency of the whole chip was a critical choice for imaging and tracking quality. The effective integration can be observed *in situ* in Figure 2. Due to PDMS's high surface energy, a high adsorption could be induced and its use was limited to the channels walls by sealing the chip on a Pyrex slide. This avoided robot adsorption, specifically during the bonding phase of the fabrication where the surfaces of the chip and the robot were chemically activated with oxygen reactive species. Another inconvenience from this material was gas permeation which caused swelling, air bubbles in the chamber and polymer release. These inconveniences are well known from the community [37]. An alternative microfluidic process that is soon to be published will be proposed to overcome usual silicon oil issues, as

well as wider thermodynamic conditions, robustness, and highly reproducible hydrodynamics characterization, using exclusively glass material.

When a magnetic field is generated on a particle containing ferromagnetic material magnetized horizontally, the generated force and torque in function of external magnetic field provides the following equation [38]

$$\mathbf{F} = \nabla(\boldsymbol{m} \cdot \boldsymbol{B}) = m_{sat}\partial_{\boldsymbol{u}} B\boldsymbol{u} \tag{1}$$

$$\tau = \mathbf{m} \times \mathbf{B} = mBsin(2(\theta_B - \theta))\boldsymbol{u} \tag{2}$$

$\mathbf{m}$ in these equations is the magnetization of the ferromagnetic parts (and m_{sat} the saturation magnetization), θ_B is the angle between the direction of the magnetic flux, $\boldsymbol{u}$ is the unit vector of the direction of the magnetic flux and $\partial_{\boldsymbol{u}}$ is the partial derivative in $\mathbf{u}$ direction. In case of planar uniform field, the generated magnetic field induces exclusively a torque – equation (2) - toward vertical axis, because of field uniformity and horizontal magnetization. The consequence is two angular positions of equilibrium on the symmetrical axis. Only one is stable and the particle magnetic moment necessarily aligns toward the field axis. The microrobotic system tends to lock with the magnetic field oscillations [39]. In case of magnetic gradients, the MagPol aligned toward flux line and achieved in-plane translational motion as can be seen in Figure 3. This force is also known as the magnetophoretic force. MagPol in-plane motion could be fully controlled by using linear combination of electromagnet's actuator [33]. Movies 1 and 2 illustrate respectively a gradient field control and a uniform rotating field.

Ni has the advantage of being cost effective, easy to process and magnetic properties are well-known, but recent literature has shown interesting results using higher magnetic susceptibility and saturation magnetization material like *Nd* rare earth alloys[40], mostly because they can reach higher magnetic power.

3.2. Magnetic control device for low Reynolds environment and heavily damped system: planar gradients or 3D uniform magnetic field

In Stokes fluid, solid dynamics are heavily damped. Therefore, any torque τ or force F applied on a particle is directly related to the particle's angular speed and the 3M follows the ordinary differential equation:

$$\gamma_z d_t \theta - \tau = 0 \tag{3}$$

$$\beta v - F = 0 \tag{4}$$

where γ_z and β are respectively the angular and linear drag coefficients, θ is the angular position and d_t is the derivative with respect to time.

Under a horizontal rotating magnetic field, the torque is oriented toward the vertical axis. If $\phi = \Omega t - \theta$ is named as the rotating phase, it turns previous equation (2) into:

$$d_t \phi + \Omega_c sin(2\phi) = \Omega \tag{5}$$

with a cut-off frequency $\Omega_C = \frac{mB}{\gamma_z}$, where m is the magnetization of the ferromagnetic layer of the robot, B the flux density of the field, Ω its pulsation and θ the particle's angular position in horizontal plane. γ_z is the drag coefficient due to fluid viscosity and substrate roughness and ϕ is the phase difference of the robot angular position with the field phase. By determining the cut-off frequency using an iterative method - described further- based on this theoretical relation, it could give access to environment parameters, as well the microrobot hydrodynamics.

Two different electromagnetic devices (Helmholtz and Maxwell coils) were considerably upgraded from former work [34, 33, 17] to achieve reproducible, highly sensitive and wide dynamic range measurement of either rotary or translational motions. It was also confirmed their inductance had a compatible time constant with the phenomenon measured - see section SI2.

3.2.1. 3 axis uniform magnetic field

Based on geometric conditions (inter-coils distance = coil radius), Figure 4 describes the Helmholtz pairs of inductors device which generated a uniform magnetic flux distribution in the central neighborhood of the coils where the fluidic chamber was lying. Based on a former optimized design, it was confirmed by a Hall effect magnetic sensors that the Helmholtz magnetic experimental platforms had a 20mm x 40mm section with less than 10 % variation of the field amplitude for each pair of coils, widely including the microfluidic chamber in this area. To obtain a sufficient sensing dynamic range, which was dependent of magnetic flux density amplitude, it was necessary to transfer as much magnetic power as possible minimizing source-robot distnce and maximizing coils' current volume.

One of the main issue with Helmholtz device is for the same voltage input a different magnetic amplitude would outcome from two different axes due to fabrication and assembly imperfections. The consequence was an ellipticity for rotating field experiments requiring calibration. Calibration and analysis were among the preliminary challenge of a Helmholtz setup. Uniformity of the magnetic field (to avoid elliptic aberration and/or $\nabla B \neq 0$) required a high fabrication and assembly precision. Compared to former work[33], it required a quantitative calibration to correct the rotating field ellipticity during circular motion. The Helmholtz coils were calibrated using Figure 5 calibration curves to minimize circular magnetic field aberration. It also confirmed the linear trend between voltage command and magnetic flux. Though highly reproducible, it can be noticed on 3^{rd} axis there was some small variations due to mechanical vibrations. The R^2 coefficient remained above 0.9992 for all axis. The axis slopes were $1mT/V$, $1.2mT/V$ and $1.5mT/V$, and each axis was normalized based on these values when generating the uniform rotating field. This calibration also confirmed magnetic flux in horizontal plan could reach up-to $12mT$ in linear regime, which to our knowledge is the double of what is currently proposed in existing literature using Helmholtz devices[14, 41].

These magnetic performances allowed us to achieve controlled tumbling motion with a simple soft ferromagnetic Ni body - see Movie 3, whereas it usually is achieved using costly $NdFeB$ body[42, 40]. In Figure SI7 the motion speed was $3.97mm/s$ i.e. $7.95 bodylength/s$, it corresponded to $\mu_{sliding} = 0.9925$.Let notices that two things directly define the speed limitation: adhesion forces and sliding friction. There is a competition between these two phenomenona and both of them limit the performances: adhesion forces, which can be overcome by a sufficient power magnetic power - see section 1.3, phase the robot out of the field and at a certain level, cannot synchronize; sliding frictions become more important as speed increases. Tumbling though, offers several advantages:

- high stability on multiple environments[40]
- vertical motion makes the microrobot able to reach narrow width area, as long as the channel depth is high enough
- if allows horizontal motion using exclusively Helmholtz device (no Maxwell coils required)

Sliding friction increase with the rotation frequency and tends to curb higher speed, as μ_s rises and limits the maximum speed. Supporting information about tumbling motion can be found in SI3.

3.2.2. 4 axis gradient magnetic field

Simple magnetophoresis (pulling force) experiences required some instrumental effort, in particular to avoid remanent magnetization and hysteresis phenomenon from the electromagnets core, and to obtain an optimal field. All details and figure about this optimization can be found in section SI2. Performing a comparative study between steel and permalloy core, it was possible to overcome these issues. It provided a way to map the gradient field generated by an electromagnet and to obtain a global value of drag coefficient β using numerical fit on the tracked positions. In cases where the experiment were disturbed by an interaction with the environment, the perturbation ϵ could be estimated

by modifying equation (4) to better understand *in-vitro* dynamics thanks to quantitative analysis.

$$\beta v - F - \epsilon = 0 \tag{6}$$

A gradient distribution was induced using a dome shaped holder containing 4 electromagnets on orthogonal axes and sharing a common center - as can be seen in Figure 6. The ability to generate a pulling force in any direction of the plane by linear superposition of the axes gradients allowed for the achievement of a movement with up to $30mT$ amplitude of field and $3mT/cm$ gradient and allowed for analysis at high frame rate – $6kframe/s$. In the heavily damped system approximation made previously, microrobot speed was directly related to the magnetic flux gradient - equations (1) and (4) - and the distribution could be directly obtained by analyzing the movement. Due to small distance from electromagnets and its high proportion of ferromagnetic part, the robot could reach the propulsion speed up to around $556mm/s$, reaching for geometry and medium viscosity the limits of low Reynolds conditions. Here the system's power is limited to "small speed" to remain in low Reynolds hypothesis, $< 20mm/s$ i.e. $Re < 10^{-2}$.

3.2.3. Open loop fast dynamics control using optical microscopy and tracking algorithm

Compared to our former system,a different camera allowing dual Camera Link interface was used. It As magnetic devices were too bulky or the lenses working distance was too small to be included in standard microscope, a custom-made microscope was used that was adapted for our study requirements. Attached on a manually controllable 6 DOF optical arm, it was possible to position anywhere without being in contact with any of the coils or sample. Reflection lighting was achieved directly from the microscope lens - Figure 7A - with an included semi-reflecting mirror. Transmission lighting was achieved from the bottom part of the setup by an optical fiber source - see Figure 7B. Though top-lighting could be an advantage because it seems more straightforward and allowed for us to notice tilt angle variations, a much better contrast and in-

tensity were observed in the transmission configuration shown in Figure 7C. Moreover, as the light is transmitted and not reflected from the robot, it avoids instability of the robot texture during tracking due to tilt variations. As fast frame rate and tracking require respectively high intensity (exposure $< 1ms$) and steady high contrast, transmission lighting was highly recommended for a fine measurement.*

The use of edge detection algorithm - see Movie 4 where edge segments were superposed in red to the original data - combined with excellent contrast and easily trackable geometry of the robot allowed to determine angular position precisely at each frame. Bulb detection allowed the detection of the robot's shape - see Movie 5 with superpose detected shape in red, the center of mass could be easily deduced from each frame. A high contrast provided by an intense transmission lighting helped to reduce instability of both tracking algorithms.

3.3. Translational motion analysis, comparative study between backward and forward motions

The microrobot in microfluidics configuration injected was prepared in 20% isopropyl alcohol. This is the same as the rotary dynamics experiments for the translational dynamics measurements. Due to the magnetization of the robot, the magnetic gradient could be evaluated in one direction. We provide in SI4 a detailed explanation of magnetization phenomenon and how we could take advantage of it for micromanipulation strategy. From the sequences and position tracking, the speed could be deduced and directly related to exerted magnetic force to obtain Figure 8. Setup vibrations, though the setup was fixed on a damped optical table, were observed as $\approx$ 1.25kHz non-negligible component.

As described in the previous section, robot polarization was controllable. Backward and forward motion of the robot were compared. A repeatable high difference was observed between backward and forward motion in terms of dynamics. Backward motion displayed in Figure 8 and 9A corresponded to the magnetic flux from theoretical distribution. Knowing the saturation magne-

tization is $m_{sat} = 0.51$MA/m, the microrobot magnetization was evaluated to be $m_{sat} = 0.51$MA/m. Magnetic gradient maximum could be evaluated $|\nabla B| =\approx 30$mT/cm and maximal magnetic force applied on MagPol could be deduced ≈ 612nN. Translational viscous drag could then be estimated to be $\beta = 6.12$nN s/μm. Forward motion precisely displays a break at 40% of trajectory ($32ms$), creating two different regimes – Figure 9B. In pre-breakdown regime, the speed increases almost linearly with only mechanical noise due to vibrations. Afterward, the speed dropped drastically and oscillated around $1.5kpix/s$ i.e. $60\mu m/s$. A change in the microrobot arm's contact with substrate could justify the appearance of a speed limit independent from the magnetic power that could be used to estimate the perturbation from substrate.

As opposed to sensing based on rotary dynamics local sensing, translational motion presented the advantage of quickly scanning horizontal plane. Here, the gradient field sensing was demonstrated by translational motion. Translational motions at the micro scale are more challenging because systems are more likely subject to unexpected interaction with imperfections and substrate interaction. Since the mass is decreased drastically (particularly in our system), huge forces i.e. accelerations are at stake in the motion of our microrobot. The consequences included difficulties to keep the robot inside field of view justifying working in a microfluidic chamber.

Another advantage of a high-speed microrobot such as MagPol is that it can achieve a higher numer of operation per seconds. The other strategy existing in the literature is to take advantage of a swarm of microrobot which is still under strong investigation [43]. In the case of magnetic microrobot, it means having a global magnetic field directing them in the same directions. It remains challenging for two reasons. First, inducing magnetization of ferromagnetic body tend to make them aggregate if they are too close or create a magnetic dipole interaction perturbing their dynamics for sensing. Second, the independent control of several robots requires more sophisticated strategy like tuning the cut off frequency of the robot using surface chemistry or different robot geometry[31], or working with different magnetization directions in a rotating magnetic field

combined with magnetic gradients.[44]

3.4. Rotary motion and breakdown phenomenon for viscosity and magnetic flux measurements

The parametric ordinary differential equation (5) was previously described by Adler et al. [39] as a quite complex behavior with a breakdown phenomenon [45, 9] at Ω_C generating two different kinetic regimes illustrated in Figure 10A simulations and with the following equations:

$$< \dot{\theta} >= \omega, \omega < \Omega_C \tag{7}$$

$$< \dot{\theta} >= \omega - \sqrt{\omega^2 - \Omega_C^2}, \omega \geq \Omega_C \tag{8}$$

where $< x >$ is the average value in time of x, θ is the robot angular position, ω the magnetic field pulsation and Ω_C the cut-off pulsation.

In locked regime, for $\omega < \Omega_C$, the robot tended quickly to a constant rotating phase $\phi = 1/2Asin(\omega/\Omega_C)$. The issue with measuring the phase was it only provided a relative value as there is an inherent undetermined delay in the control loop of any 3M. At higher frequency > 1kHz, the robot did not respond with our device maximal power and the system was considered as mute. Equation (5) can be exploited in a variety of sensing applications summed up in Table 1.

The Figure 10B compares a simulated frequency response using Runge-Kutta method with an experimental average rotary frequency clearly describing a transition at 98Hz.It fit with the expected proportional dependency between magnetic power and cut-off frequency. It seemed that above cut-off frequency, the experimental response dropped faster than in theory. As it was at micro-metric scale, in chaotic regime, the contribution of electrostatic and capillary forces absorbed too much energy for equation 5 to be verified and a perturbation term should be included.

The rotary dynamics were first applied to measure the external magnetic field intensity. The robot ($450 \times 400 \times 7\mu\text{m}^3$) was used inside microfluidic chamber

$(3300 \times 2200 \times 280\mu\text{m}^3)$ configuration as shown in Figure 2 for this measurement. Isopropyl alcohol with the same concentration for each measurement was injected to the microfluidic chamber. The planar circular rotating field was generated with a frequency varying from 1 to 150Hz with 10Hz incremental step, then zoomed in the breakdown area with a 1Hz step. The dynamics could be analyzed with up to 40 images per revolution at maximal frequency (frame rate $>$ 6kHz). The angular speed was then integrated to obtain an average rotation rate. The measurements were repeated with different power inputs (each time calibrated i.e. inducing minimized ellipticity). The algorithm is summed up in Figure 11 and Movie 6 sums it up in the case of a 98Hz cut-off frequency. It also confirms the limit of detection of Ω_C is at least 1 Hz.

Figure 12 shows the measured cut-off frequencies in function of the electromagnetic field intensities. If the sensibility of the system is defined as the variation of Ω_C depending on the power, an experimental value was obtained of 24.22rad/(s mT). Since nickel is a soft ferromagnetic material of known initial susceptibility $\chi_i = 109$ (unitless) and saturation $m_{sat} = 0.51 \times 10^6 A/m$ [38], two asymptotic regimes were expected:one fitting a linear response giving us the ratio between magnetization and viscosity ratio and confirming that the material at this point is magnetized. If the required power to start is approximately known, fewer points are necessary to determine the coefficient of the line. The first qualitative result was the confirmation that the robot was magnetized over 3mT flux, the cut-off frequency being proportional to B concomitantly to (9). From (5), it is directly proportional to the magnetic flux $\Omega_C = (m_{sat}B)/\gamma_z$. Considering equations (7) and (8), a non-magnetized robot would have had a quadratic variation with the magnetic flux $\Omega_C = (\chi_i B^2)/(\mu_0 \gamma_z)$. Quantitative information was also obtained that allows, as the Ni saturation value is typically$0.51 \times 10^6 A/m$ at ambient temperature, to approximate the value of the damping coefficient.

$$m \approx \frac{\chi_i B}{\mu_0}, B \ll B_C \tag{9}$$

$$m = m_{sat}, B \gg B_C \tag{10}$$

The same principle could be applied to measure the viscosity of liquid. The same setup was used varying the renewal of the liquid environment. The viscosities of three different liquids were successfully related to cut-off frequencies. The magnetic field intensity was fixed to 3.06mT to guarantee a constant power in saturated regime (Figure 12). The measurements were repeated for three different viscosities at a fixed magnetic power, using the same post treatment process. Figure 13 displays the measured cut-off frequencies in function of different liquid viscosities. The magnetic flux was maintained constant, which defines the sensibility of the system as the variation of Ω_C is a linear function of it. An experimental slope of 118.1cP/s was obtained. As the response was approximately linear (constant $b = 0.04\text{cP} \ll \nu$ liquid), the contribution from substrate and interface phenomenon in dynamic regime was apparently negligible compared to the viscosity drag in dynamic regime.

The potential fabrications errors of the magnetic instruments are overcome thanks to the magnetic calibration curve. Fixing hydrodynamic (viscosity and ionic force of the medium) and magnetic (field power) parameters, the relative variation of rotary dynamics cut-off frequency Ω_c the influence of substrate impurity could be deduced and steady rotational motion was observed despite environmental noise. As the chamber is flushed between each experiment with a mixture of degassed isopropyl alcohol and water, it was free of debris and bubbles. The only perturbation observable then came from the substrate imperfections but the experience in permanent regime, i.e. when the robot is locked with the rotary field, seemed to lead to a negligible contribution of substrate.

3.5. Transition dynamics analysis to study robot-surface interactions

As former analysis seemed to confirm surface interaction is negligible on the 3M dynamics additionally to the viscous drag, we finally investigated the dynamics transition related to a constant uniform magnetic flux.

First, using a horizontally oscillating single axis field, we observed the time-response of robot varying the magnetic flux amplitude, tracking the angular position to precisely access the angular position function of time. A gate function of average value 0 and $2.5Hz$ frequency was generated toward x and we sweeped amplitude from 0 to 15 mT. This frequency was sufficient to reach the stable equilibrium position, and allowed to observe three cases of time response. Below $0.8mT$, the microrobot remained static which means the static friction was too high compared to magnetic flux to overcome. Between $0.8mT$ and $3mT$, we started observing an oscillation between the two stable equilibrium at each period. At 0.8mT, it took approximately $2s$ i.e. $4cycles$ - see Figure 14a and Movie 4. Interestingly, these angular positions increases progressively until reaching the π value which means the dynamic friction decreases with time until becoming negligible. This confirms an evolution of the microrobot-surface interaction. It was not observed in the breakdown phenomenon as a rotating field and not a gate was induced. The robot oscillation displayed a blocked and no observable transition is observed, which means the magnetic force is sufficient to change in one oscillation the nature of contact. In the second case, when amplitudes varied between $3mT$ to up-to $11mT$, the transition to oscillating regime was spontaneous as can be seen on Figure 14B, meaning the dynamic adhesion could be overcome at the first cycle.

These experiments confirmed that there was indeed an inherent interaction substrate-robot, but that this contribution was overcome once the transition regime was reached. It also provided a limitation of rotary sensing, as for power below $0.8mT$, the magnetic torque was not sufficient to observe the breakdown phenomenon, the 3M could not overcome the substrate static friction and adhesion forces. Former studies like Pawashe et al. have attempted to describe friction, adhesion and damping from external environment of a 3M[46], this study offers a complementary approach to experiment and determine limitations induced by these phenomenon.

4. Conclusion

It was demonstrated here that remotely powered microrobotic swimmers integrated to microfluidic devices may not only be used for physical manipulations like cargo transport, but also serve as wireless physical sensors with the proper magnetic control system. Taking advantage of the polarization of the 3M ferromagnetic body, an original micromanipulation strategy was demonstrated as well as remote sensing.

Analyzing elementary rotation and translation displacements could give access to hydrodynamic parameters such as viscous drag η and shape factor κ of 3M, as well as magnetic parameters such as magnetic susceptibility χ. The translational sensing by polarizable motion capability could estimate the local perturbations or viscous drags.

These analysis also could provide quantification of the interaction between the 3M and the microfluidic substrate. The substrate imperfections and adhesion forces seemed to not have a critical impact in the breakdown phenomenon measurement, however they impacted the transition dynamics and revealed a limitation in terms of magnetic power. The maximum magnetic power was inherent to the magnetic control device, whereas the minimum for sensing was related to substrate imperfections and adhesion force. Future investigation to deduce the influence of roughness and adhesion force could be investigated.

Both rotary and translational sensing, combined with automated motions, may be used in dynamically building physical maps inside microfluidic environments where there are challenges to integrate additional sensors. In future implementations, the power of magnetic field sensing and viscosity sensing could be applied to detect a wide range of external physical conditions (thermally, chemically, or biologically) by increasing the sensing range and resolution through automated sensing and design optimizations. For example, integrating a thermostated stage in the experimental device could confirm the 3M capacity to estimate an estimation of local temperature measuring the viscosity, as it is function of temperature, of a known media (such as DI water, or isopropyl

alcohol).

Acknowledgements

The material is based on work supported by the French National Research Agency under grant ANR-11-JS03-0002. Any opinions, findings, and conclusions or recommendations expressed in this material are those of the authors and do not necessarily reflect the views of the French National Research Agency. For her support and fruitful discussions on the manuscript, the authors gratefully acknowledge Celine Agnes. The authors also acknowledge LPN cleanroom staffs in particular S. Guilet, L. Ferlazzo, and C. Roblin for microfabrication advices. H. S. thanks C. Gosse and S. Barbay for fruitful discussions.

References

[1] B. J. Nelson, I. K. Kaliakatsos, J. J. Abbott, Microrobots for minimally invasive medicine, Annual Review of Biomedical Engineering 12 (2010) 55–85. doi:10.1146/annurev-bioeng-010510-103409.

[2] X.-Z. Chen, M. Hoop, F. Mushtaq, E. Siringil, C. Hu, B. J. Nelson, S. Pané, Recent developments in magnetically driven micro- and nanorobots, Applied Materials Today 9 (2017) 37–48. doi:10.1016/j.apmt.2017.04.006.
URL http://www.sciencedirect.com/science/article/pii/S2352940717300379

[3] P. Serrano, D. Decanini, L. Leroy, L. Couraud, G. Hwang, Multiflagella artificial bacteria for robust microfluidic propulsion and multimodal micromanipulation, Microelectronic Engineering 195 (2018) 145–152. doi:10.1016/j.mee.2018.04.003.
URL http://www.sciencedirect.com/science/article/pii/S0167931718301473

[4] J. J. Abbott, M. C. Lagomarsino, L. Zhang, L. Dong, B. J. Nelson, How Should Microrobots Swim?, The International Journal of Robotics

Researchdoi:10.1177/0278364909341658.
URL http://ijr.sagepub.com/content/early/2009/07/21/0278364909341658

[5] S. Martel, W. Andre, M. Mohammadi, Z. Lu, O. Felfoul, Towards swarms of communication-enabled and intelligent sensotaxis-based bacterial microrobots capable of collective tasks in an aqueous medium, in: IEEE International Conference on Robotics and Automation, 2009. ICRA '09, 2009, pp. 2617–2622. doi:10.1109/ROBOT.2009.5152588.

[6] P. P. Lele, B. G. Hosu, H. C. Berg, Dynamics of mechanosensing in the bacterial flagellar motor, Proceedings of the National Academy of Sciences 110 (29) (2013) 11839–11844. doi:10.1073/pnas.1305885110.
URL http://www.pnas.org/content/110/29/11839

[7] S. Alvo, Etude, modélisation et mesure des forces d'adhésion à l'échelle microscopique., Ph.D. thesis, Université Pierre et Marie Curie - Paris VI (Oct. 2012).
URL http://tel.archives-ouvertes.fr/tel-00772533

[8] N. Chaillet, S. Régnier, Microrobotics for Micromanipulation, 1st Edition, Wiley-ISTE, London, UK : Hoboken, NJ, 2010.

[9] E. Guyon, J.-P. Hulin, L. Petit, Hydrodynamique physique, 3rd Edition, CNRS Editions, Les Ulis, 2012.

[10] P. Tabeling, Introduction to microfluidics, Oxford University Press, Oxford, U.K. ; New York, 2005.

[11] A. Barbot, D. Decanini, G. Hwang, On-chip Microfluidic Multimodal Swimmer toward 3d Navigation, Scientific Reports 6 (2016) 19041. doi:10.1038/srep19041.
URL https://www.nature.com/articles/srep19041

[12] A. Barbot, D. Decanini, G. Hwang, The Rotation of Microrobot Simplifies 3d Control Inside Microchannels, Scientific Reports 8 (1) (2018) 438. doi:

10.1038/s41598-017-18891-w.
URL https://www.nature.com/articles/s41598-017-18891-w

[13] M. Hagiwara, T. Kawahara, Y. Yamanishi, T. Masuda, L. Feng, F. Arai, On-chip magnetically actuated robot with ultrasonic vibration for single cell manipulations, Lab on a Chip 11 (12) (2011) 2049–2054. doi:10.1039/C1LC20164F.
URL http://pubs.rsc.org/en/content/articlelanding/2011/lc/c1lc20164f

[14] T. Petit, L. Zhang, K. E. Peyer, B. E. Kratochvil, B. J. Nelson, Selective Trapping and Manipulation of Microscale Objects Using Mobile Microvortices, Nano Letters 12 (1) (2012) 156–160. doi:10.1021/nl2032487.
URL https://doi.org/10.1021/nl2032487

[15] M. Hagiwara, T. Kawahara, F. Arai, Local streamline generation by mechanical oscillation in a microfluidic chip for noncontact cell manipulations, Applied Physics Letters 101 (7) (2012) 074102. doi:10.1063/1.4746247.
URL https://aip.scitation.org/doi/abs/10.1063/1.4746247

[16] E. K. Sackmann, A. L. Fulton, D. J. Beebe, The present and future role of microfluidics in biomedical research, Nature 507 (7491) (2014) 181–189. doi:10.1038/nature13118.
URL https://www.nature.com/articles/nature13118

[17] G. Hwang, I. A. Ivan, J. Agnus, H. Salmon, S. Alvo, N. Chaillet, S. Régnier, A.-M. Haghiri-Gosnet, Mobile microrobotic manipulator in microfluidics, Sensors and Actuators A: Physical 215 (2014) 56–64. doi:10.1016/j.sna.2013.09.030.
URL http://www.sciencedirect.com/science/article/pii/S0924424713004792

[18] T. Kawahara, M. Sugita, M. Hagiwara, F. Arai, H. Kawano, I. Shihira-Ishikawa, A. Miyawaki, On-chip microrobot for investigating the response

of aquatic microorganisms to mechanical stimulation, Lab on a Chip 13 (6) (2013) 1070–1078. doi:10.1039/C2LC41190C.
URL http://pubs.rsc.org/en/content/articlelanding/2013/lc/c2lc41190c

[19] S. Sakuma, B. Turan, F. Arai, High throughput mechanical characterization of oocyte using robot integrated microfluidic chip, in: 2013 IEEE/RSJ International Conference on Intelligent Robots and Systems (IROS), 2013, pp. 2047–2052. doi:10.1109/IROS.2013.6696630.

[20] S. Sakuma, K. Kuroda, C.-H. D. Tsai, W. Fukui, F. Arai, M. Kaneko, Red blood cell fatigue evaluation based on the close-encountering point between extensibility and recoverability, Lab on a Chip 14 (6) (2014) 1135–1141. doi:10.1039/C3LC51003D.
URL http://pubs.rsc.org/en/content/articlelanding/2014/lc/c3lc51003d

[21] J. Abadie, C. Roux, E. Piat, C. Filiatre, C. Amiot, Experimental measurement of human oocyte mechanical properties on a micro and nanoforce sensing platform based on magnetic springs, Sensors and Actuators B: Chemical 190 (2014) 429–438. doi:10.1016/j.snb.2013.08.042.
URL http://www.sciencedirect.com/science/article/pii/S0925400513009660

[22] A. Barbot, D. Decanini, G. Hwang, Helical microrobot for force sensing inside microfluidic chip, Sensors and Actuators A: Physical 266 (2017) 258–272. doi:10.1016/j.sna.2017.09.004.
URL http://www.sciencedirect.com/science/article/pii/S0924424717303709

[23] K. B. Yesin, K. Vollmers, B. J. Nelson, Actuation, Sensing, and Fabrication for In Vivo Magnetic Microrobots, in: Experimental Robotics IX, Springer Tracts in Advanced Robotics, Springer, Berlin, Heidelberg, 2006, pp. 321–

330. doi:10.1007/11552246_31.
URL https://link.springer.com/chapter/10.1007/11552246_31

[24] H. Maruyama, F. Arai, T. Fukuda, On-chip pH measurement using functionalized gel-microbeads positioned by optical tweezers, Lab on a Chip 8 (2) (2008) 346–351. doi:10.1039/b712566f.

[25] O. Ergeneman, G. Chatzipirpiridis, J. Pokki, M. Marin-Suárez, G. A. Sotiriou, S. Medina-Rodriguez, J. F. F. Sanchez, A. Fernandez-Gutiérrez, S. Pane, B. J. Nelson, In Vitro Oxygen Sensing Using Intraocular Microrobots, IEEE Transactions on Biomedical Engineering 59 (11) (2012) 3104–3109. doi:10.1109/TBME.2012.2216264.
URL http://ieeexplore.ieee.org/document/6291753/

[26] P. J. Wyatt, Light scattering and the absolute characterization of macromolecules, Analytica Chimica Acta 272 (1) (1993) 1–40. doi:10.1016/0003-2670(93)80373-S.
URL http://www.sciencedirect.com/science/article/pii/0003267093803735

[27] J. Lipfert, M. M. van Oene, M. Lee, F. Pedaci, N. H. Dekker, Torque Spectroscopy for the Study of Rotary Motion in Biological Systems, Chemical Reviews 115 (3) (2015) 1449–1474. doi:10.1021/cr500119k.
URL https://doi.org/10.1021/cr500119k

[28] I. Etchart, H. Chen, P. Dryden, J. Jundt, C. Harrison, K. Hsu, F. Marty, B. Mercier, MEMS sensors for density–viscosity sensing in a low-flow microfluidic environment, Sensors and Actuators A: Physical 141 (2) (2008) 266–275. doi:10.1016/j.sna.2007.08.007.
URL http://www.sciencedirect.com/science/article/pii/S0924424707005924

[29] I. Sinn, T. Albertson, P. Kinnunen, D. N. Breslauer, B. H. McNaughton, M. A. Burns, R. Kopelman, Asynchronous Magnetic Bead Rotation Microviscometer for Rapid, Sensitive, and Label-Free Studies of Bacterial

Growth and Drug Sensitivity, Analytical Chemistry 84 (12) (2012) 5250–5256. doi:10.1021/ac300128p.
URL https://doi.org/10.1021/ac300128p

[30] Y. Li, K. R. Ward, M. A. Burns, Viscosity Measurements Using Microfluidic Droplet Length, Analytical Chemistry 89 (7) (2017) 3996–4006. doi:10.1021/acs.analchem.6b04563.
URL https://doi.org/10.1021/acs.analchem.6b04563

[31] X. Wang, C. Hu, L. Schurz, C. De Marco, X. Chen, S. Pané, B. J. Nelson, Surface-Chemistry-Mediated Control of Individual Magnetic Helical Microswimmers in a Swarm, ACS Nano 12 (6) (2018) 6210–6217. doi:10.1021/acsnano.8b02907.
URL https://doi.org/10.1021/acsnano.8b02907

[32] R. Pieters, H. Tung, S. Charreyron, D. F. Sargent, B. J. Nelson, RodBot: A rolling microrobot for micromanipulation, in: 2015 IEEE International Conference on Robotics and Automation (ICRA), 2015, pp. 4042–4047. doi:10.1109/ICRA.2015.7139764.

[33] H. Salmon, L. Couraud, G. Hwang, Using breakdown phenomenon as mobile magnetic field sensor in microfluidics, in: 2013 IEEE/RSJ International Conference on Intelligent Robots and Systems (IROS), 2013, pp. 2041–2046. doi:10.1109/IROS.2013.6696629.

[34] H. Salmon, L. Couraud, G. Hwang, Swimming property characterizations of Magnetic Polarizable microrobots, in: 2013 IEEE International Conference on Robotics and Automation (ICRA), 2013, pp. 5520–5526. doi:10.1109/ICRA.2013.6631369.

[35] C. A. Schneider, W. S. Rasband, K. W. Eliceiri, NIH Image to ImageJ: 25 years of Image Analysis, Nature methods 9 (7) (2012) 671–675.
URL https://www.ncbi.nlm.nih.gov/pmc/articles/PMC5554542/

[36] E. Marchand, F. Chaumette, Feature tracking for visual servoing purposes, Robotics and Autonomous Systems 52 (1) (2005) 53–70.
URL http://hal.inria.fr/inria-00351898

[37] E. Roy, A. Pallandre, B. Zribi, Marie-Charlotte Horny, F. D. Delapierre, A. Cattoni, J. Gamby, A.-M. Haghiri-Gosnet, Overview of Materials for Microfluidic Applications, in: X.-Y. Yu (Ed.), Advances in Microfluidics, IntechOpen, Rijeka, 2016. doi:10.5772/65773.
URL https://doi.org/10.5772/65773

[38] D. C. Jiles, Introduction to Magnetism and Magnetic Materials, Second Edition, CRC Press, 1998.

[39] R. Adler, A study of locking phenomena in oscillators, Proceedings of the IEEE 61 (10) (1973) 1380–1385. doi:10.1109/PROC.1973.9292.

[40] C. Bi, M. Guix, B. Johnson, W. Jing, D. Cappelleri, C. Bi, M. Guix, B. V. Johnson, W. Jing, D. J. Cappelleri, Design of Microscale Magnetic Tumbling Robots for Locomotion in Multiple Environments and Complex Terrains, Micromachines 9 (2) (2018) 68. doi:10.3390/mi9020068.
URL https://www.mdpi.com/2072-666X/9/2/68

[41] Z. Ye, M. Sitti, Dynamic trapping and two-dimensional transport of swimming microorganisms using a rotating magnetic microrobot, Lab on a Chip 14 (13) (2014) 2177–2182. doi:10.1039/C4LC00004H.
URL https://pubs.rsc.org/en/content/articlelanding/2014/lc/c4lc00004h

[42] W. Jing, N. Pagano, D. J. Cappelleri, A novel micro-scale magnetic tumbling microrobot, Journal of Micro-Bio Robotics 8 (1) (2013) 1–12. doi:10.1007/s12213-012-0053-1.
URL https://doi.org/10.1007/s12213-012-0053-1

[43] S. Chowdhury, W. Jing, D. J. Cappelleri, Controlling multiple microrobots: recent progress and future challenges, Journal of Micro-Bio Robotics 10 (1)

(2015) 1–11. doi:10.1007/s12213-015-0083-6.
URL https://doi.org/10.1007/s12213-015-0083-6

[44] E. Diller, J. Giltinan, P. Jena, M. Sitti, Three dimensional independent control of multiple magnetic microrobots, in: 2013 IEEE International Conference on Robotics and Automation (ICRA), 2013, pp. 2576–2581. doi:10.1109/ICRA.2013.6630929.

[45] F. Pedaci, Z. Huang, M. van Oene, S. Barland, N. H. Dekker, Excitable particles in an optical torque wrench, Nature Physics 7 (3) (2011) 259–264. doi:10.1038/nphys1862.
URL http://www.nature.com/nphys/journal/v7/n3/full/nphys1862.html

[46] C. Pawashe, S. Floyd, M. Sitti, Modeling and Experimental Characterization of an Untethered Magnetic Micro-Robot, The International Journal of Robotics Research 28 (8) (2009) 1077–1094. doi:10.1177/0278364909341413.
URL https://doi.org/10.1177/0278364909341413

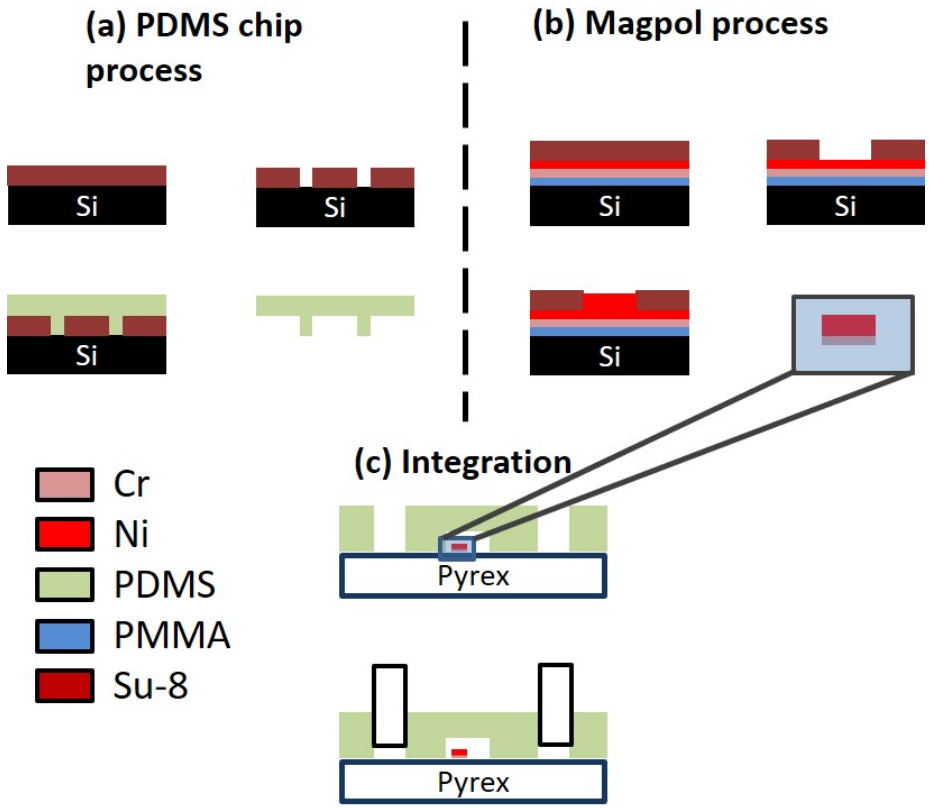

Figure 1: Schematic of microfabrication and chip process and integration.

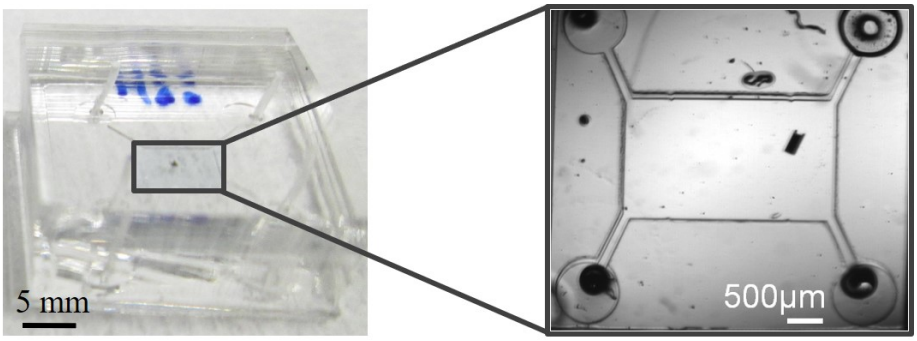

Figure 2: Photos of microfluidic chip and embedded microrobot.

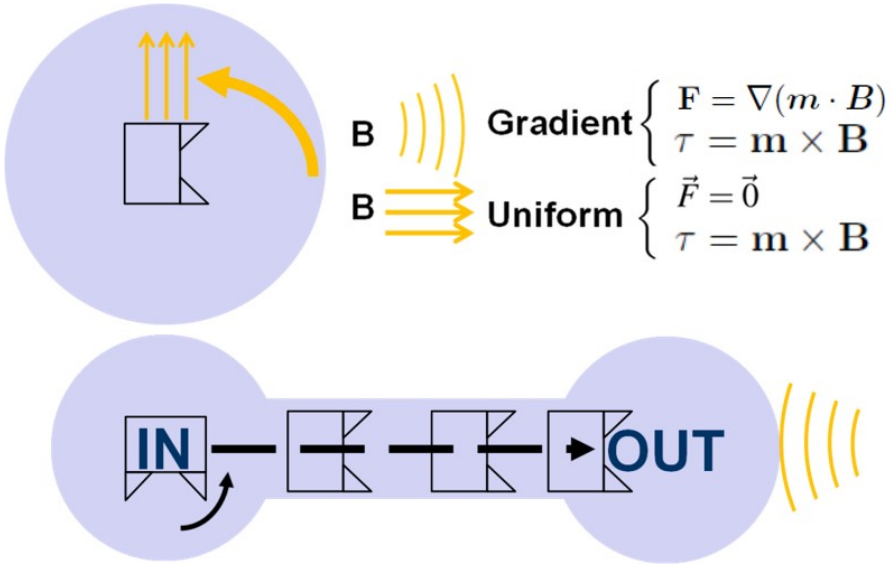

Figure 3: Principle of remote magnetic control (photo with schematics for rotary and translational motions). Two types of magnetic actuation depending on the field distribution.

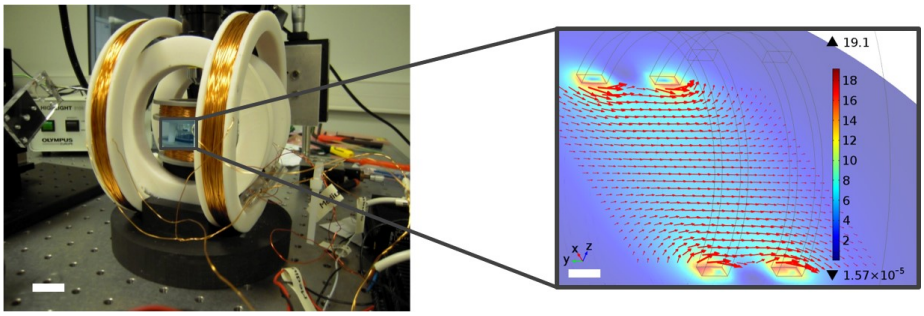

Figure 4: Experimental setup for uniform magnetic field control. Photo of the 3D-Helmholtz device and corresponding magnetic flux distribution of one axis simulated by FEM. Scale bar is equivalent to $25mm$. Map colors correspond to magnetic flux amplitude (in mT) for a constant current input. Red arrows indicate streamlines. Scale bar is equivalent to $15mm$.

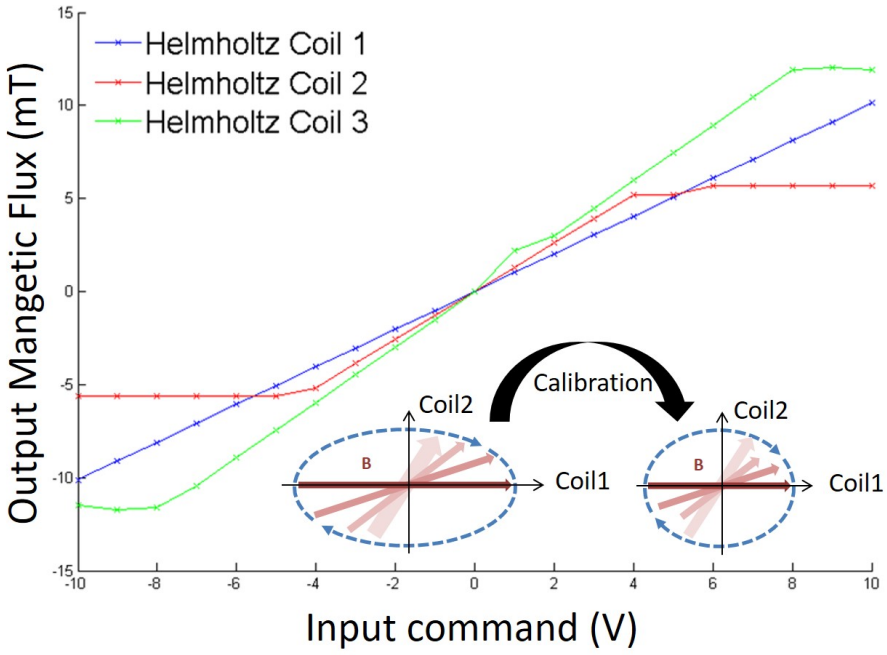

Figure 5: Calibration curves of the three pairs of Helmholtz coils device. Big coils axis x is the red line, medium coils axis y is the green line and small coils axis z is the blue line. The schematic describes a rotating uniform magnetic field after calibration. For each curve, $R^2 > 0.9992$.

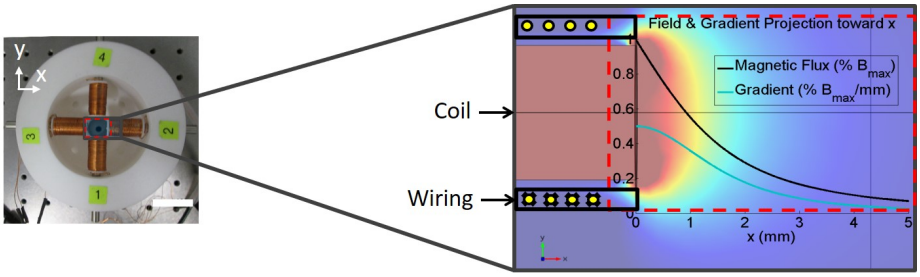

Figure 6: Experimental setup for gradient control. Photo of the dome shaped device and corresponding magnetic flux distribution of one axis simulated by finite element method (FEM). Color corresponds to magnetic flux amplitude for a constant current input. Green curve corresponds to magnetic flux gradient x-component on the solenoid axis, black curve to magnetic flux x-component on the solenoid axis as well. Scale bar is equivalent to $25mm$.

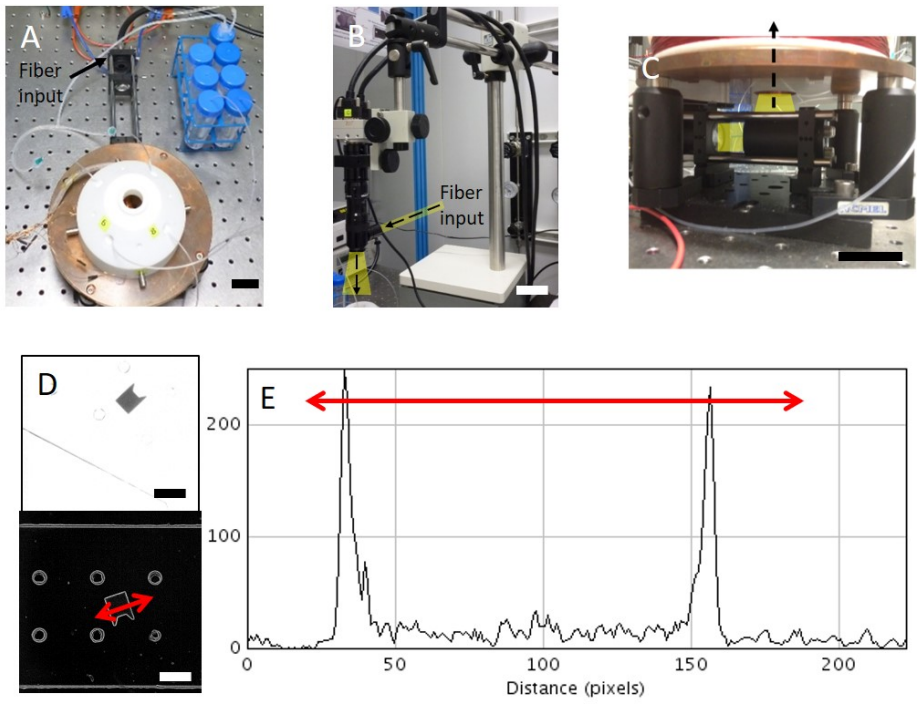

Figure 7: (A) Top view photo of of the dome device on its optomechanical support. Fluidic chip is connected to 50mL tank and bottom lighting setup beginning can be observed. (B) Photo of top lighting using a side light injection with a semi reflecting mirror integrated to the zoom lens. (C) Photo of bottom lighting optical setup on bottom of our device. (D) Photos of transmission lighting microscopy and associated Sobel transform (gradient method), red arrow defines the plotted profile on D. (E) Intensity profile with red arrow corresponding to C picture. The edges contrast could be observed compared to background and noise. Scale bar for (A) (B) and (C) are equivalent to $25mm$, (D) is equivalent to $500\mu m$.

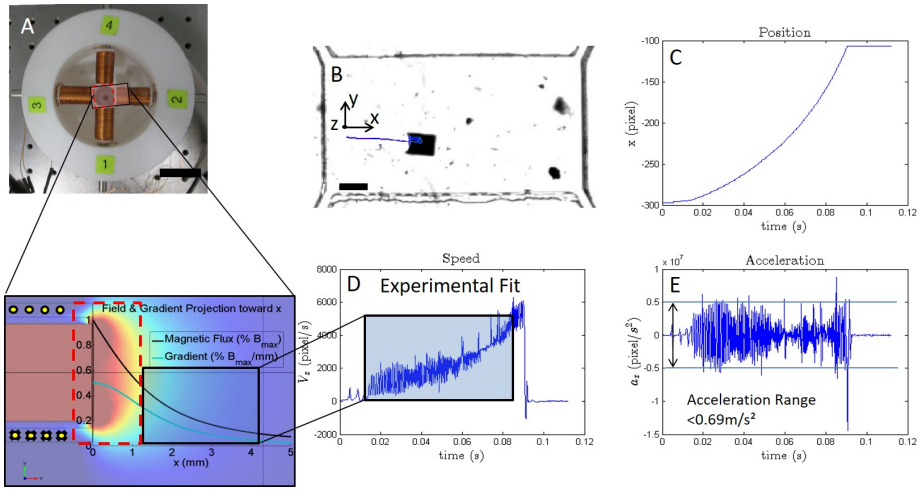

Figure 8: Translational dynamics analysis and sensing using gradient magnetic fields. (A), Gradient field setup and distribution of magnetic flux (norm) from solenoid is proportional to magnetic force generated on microrobot, thus its speed. (A) scale bar is equivalent to $25mm$, (B) to $500\mu m$. (B-E), High-temporal tracking and detected position of translational motion by local magnetic field gradients. $20\mu m/pix$. Trajectories analysis and comparison with magnetic gradient (FEM).

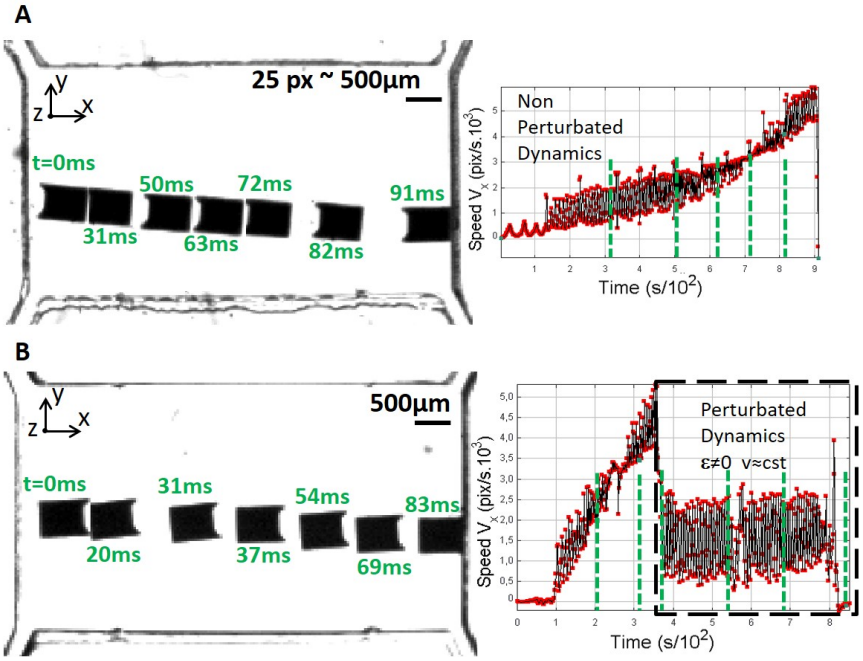

Figure 9: Comparative study of backward and forward motions. (A)Superposed photos of trajectory at different positions with associated speed distribution extracted from position tracking. Green dotted lines indicate superposed positions. Backward motion displays expected dynamics from model. (B) Superposed photos of forward motion. We clearly notice a split into two different regimes.

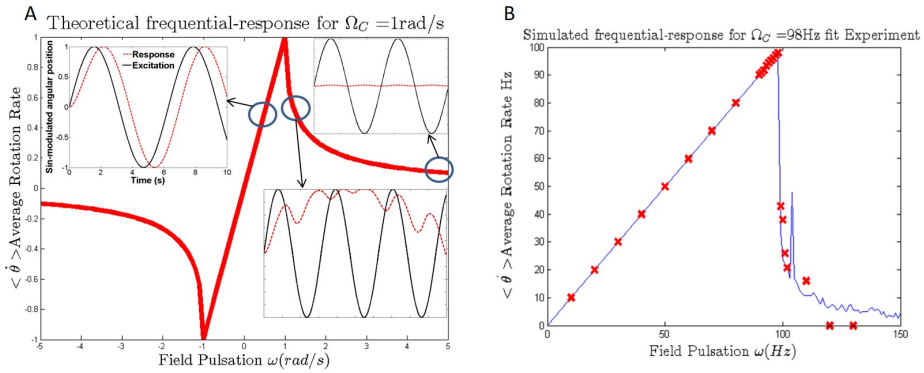

Figure 10: Rotary dynamics-based sensing(A) Average rotation rate from equation (7) and (8) - displaying breakdown phenomenon - and temporal responses simulated using ODE solver. Asymptotic frequency responses to rotating magnetic fields can be described by (6) and (7); each regime typical temporal response is illustrated by the sin-modulated angular orientation of robot - in black – and B field in red. (B) Comparison of simulated solutions (Runge-Kutta method) in continuous line and experimental (with tracking) frequency- response marked point – with a 1 Hz precision. First scan is 10 Hz step. Second, centered around the cut-off frequency, is 1 Hz.

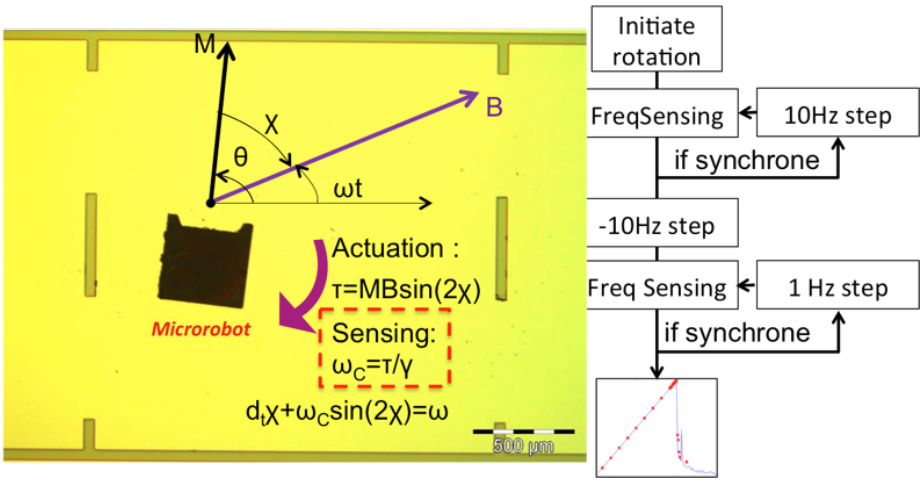

Figure 11: Photo of a microrobot in a fluidic chamber displaying in black its magnetization m and in purple B the applied magnetic flux. The purple curved arrow indicates the rotation direction. On the right, the flowchart indicates the detection algorithm to determine cut-off frequency Ω_c in the context of uniform planar rotating field.

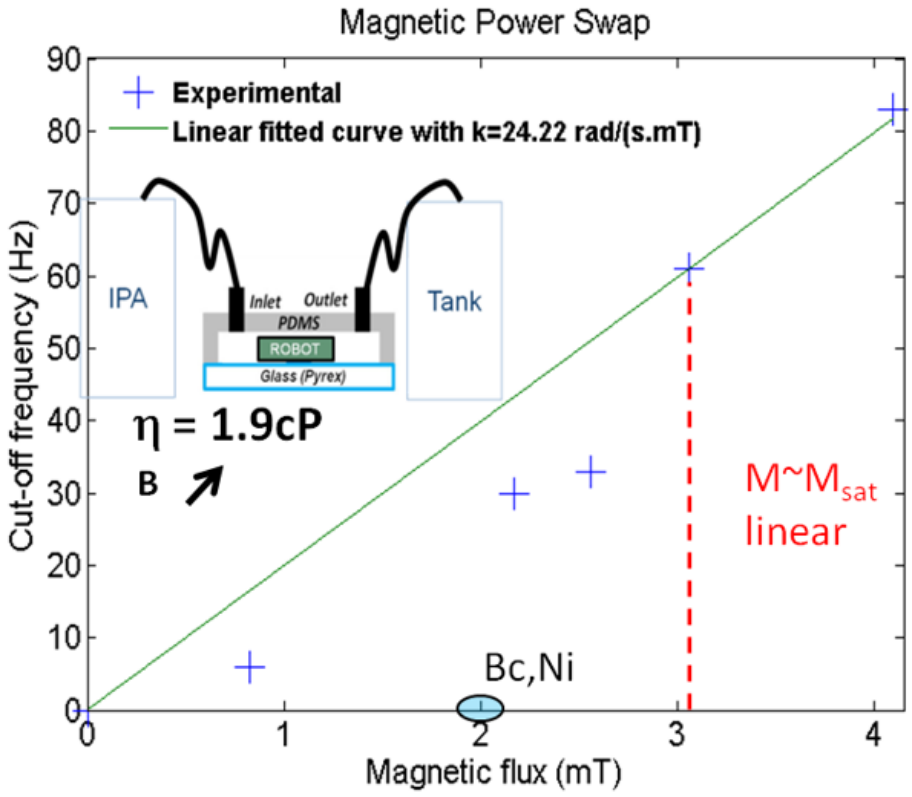

Figure 12: Cut-off frequency function of magnetic field amplitude in fixed $1.9cP$ viscosity medium, with linear fitting using least-square method in saturated domain.

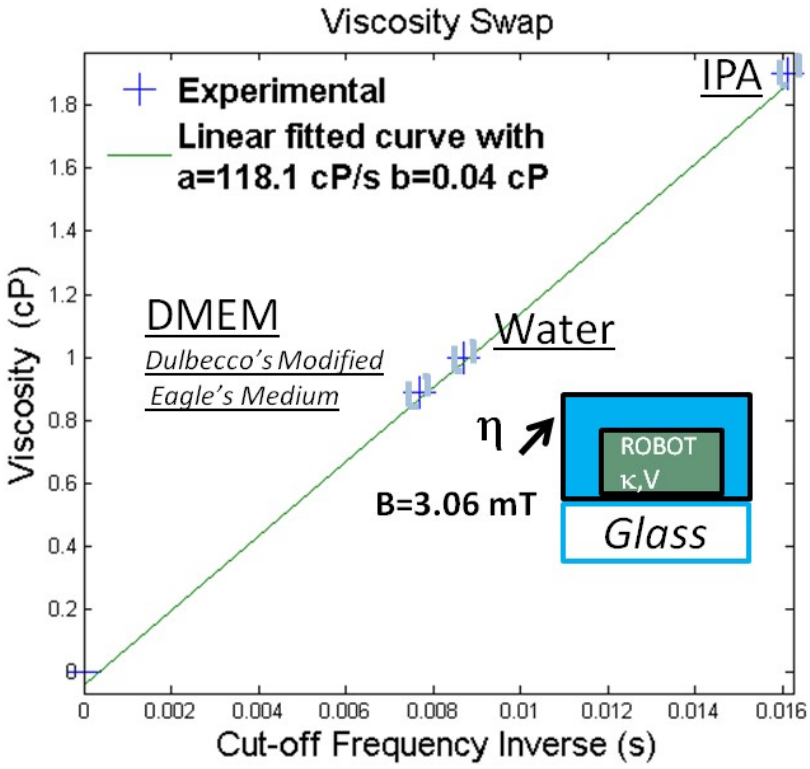

Figure 13: Viscosity function of cut-off frequency Inverse at a fixed magnetic power of $3.06mT$, with linear fitting in green.

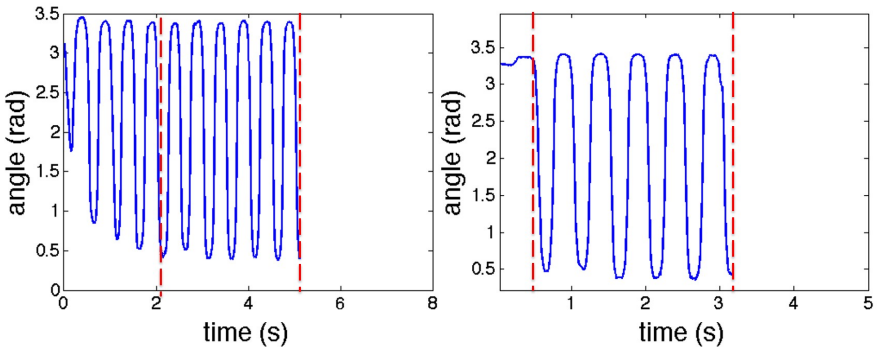

Figure 14: Blue curve displays the measured angular position, under a $0.8mT$ (left) and a $3mT$ (right) uniform magnetic field toward x axis. The two dashed red lines indicates when the oscillations reach permanent regime.

Table 1: Sensing applications depending on the fixed parameters, $\Omega_c = \frac{mB}{\gamma_z}$

fixed parameters	variable	application
B, γ_z	m	magnetic moment, ferromagnetic body uniformity
m, γ_z	B	local magnetic flux
B, m	γ_z	viscous drag, local viscosity, 3M shape influence

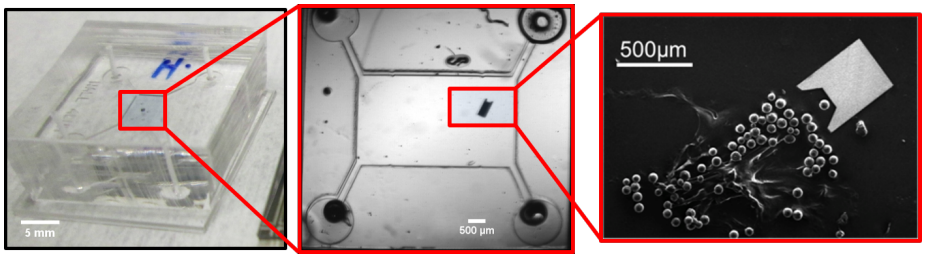

Graphical abstract.